JACS
JOURNAL OF THE AMERICAN CHEMICAL SOCIETY

Article

pubs.acs.org/JACS

Photocatalytic Reaction Centers in Two-Dimensional Titanium Oxide Crystals

Shintaro Ida,*[,†,§,#] Namhoon Kim,[‡,#] Elif Ertekin,*[,‡,#] Sakae Takenaka,[¶,§,#] and Tatsumi Ishihara[†,#]

[†]Department of Applied Chemistry, Graduate School of Engineering, Kyushu University, 744 Motooka, Nishi-ku, Fukuoka 819-0395, Japan

[‡]Department of Mechanical Science and Engineering, University of Illinois at Urbana—Champaign, Urbana, Illinois 61801, United States

[¶]Department of Chemical Engineering, Graduate School of Engineering, Kyushu University, Fukuoka 819-0395, Japan

[§]PRESTO, Japan Science and Technology Agency (JST), 4-1-8 Honcho Kawaguchi, Saitama 332-0012, Japan

[#]International Institute for Carbon Neutral Energy Research (I2CNER), Kyushu University, Fukuoka 819-0395, Japan

Supporting Information

ABSTRACT: Co-catalysts play an important role in photocatalytic water splitting. The co-catalyst is generally deposited in the form of nanoparticles on the catalyst surface, and is believed to provide water oxidation and reduction sites. However, the minimum size of a co-catalyst that can function as a reaction site and the detailed local environment of the photocatalytic reaction centers are not yet fully understood. Here, we show that even isolated single-atom Rh dopants in two-dimensional titanium oxide crystals can effectively act as co-catalysts for the water-splitting reaction. At an optimal doping concentration, the hydrogen production rate is increased substantially in comparison to that found with the undoped crystals. We also present first-principles simulations based on density functional theory to provide insights into the atomic-scale mechanism by which the isolated Rh dopants induce changes to the dissociation reaction energy landscape. These results provide new insights for better understanding the role of the co-catalyst in the photocatalytic reaction.

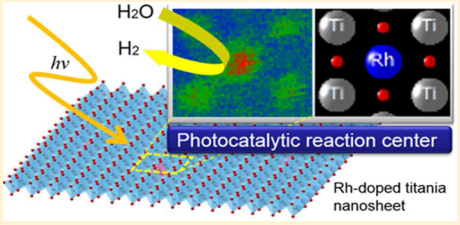

INTRODUCTION

Hydrogen production from water using solar energy is a long-standing goal of renewable energy research.[1−5] The splitting of water into hydrogen and oxygen using the energy of photoexcited carriers generated in semiconducting powders, generally called photocatalysts, is one promising approach.[2,6,7] Advances to photocatalytic technology over the past decade have made water splitting possible using only the visible part of the solar spectrum.[7−9] Interestingly, the oxidation and reduction reactions both proceed on the same small particles, with diameters ranging from several hundred nanometers to several micrometers. This is accomplished by loading co-catalyst nanoparticles on the semiconducting particles.[10] The co-catalysts are thought to act as reduction and/or oxidation sites, but many aspects such as the reaction mechanism and the structure of the reaction site remain unclear. This is partly because the structure is too complex to easily identify water adsorption sites, with the polycrystalline cocatalyst nanoparticles randomly deposited on the various crystal faces of the semiconducting power. Therefore, much simpler crystal systems and/or more controlled surface conditions can help precisely identify the role of the co-catalyst in photocatalytic water splitting.

Our research has focused on two-dimensional nanocrystals with a thickness of around 1 nm, which are called nanosheets.[11−17] With their high surface area-to-volume ratio, nanosheets provide an ideal photocatalyst structure for determining the reaction mechanisms. Nanosheets can be obtained by exfoliating a layered oxide material composed of single-crystal layers of the same thickness that expose the same crystal face to the reaction solvent. For example, for a calcium niobate ($Ca_2Nb_3O_{10}$) nanosheet, the layer thickness is approximately 1 nm and the exposed crystal face is (001)-oriented.[18] When doped, due to the low thickness and high surface area-to-volume ratio, all dopants are expected to be present very close to the surface. Therefore, most of the dopants can be directly involved in the catalytic reaction, potentially influencing or improving photocatalytic activity in the same manner as in traditional co-catalyst loading. However, there is no clear evidence yet if (and if so, how) single-atom dopants function as photocatalytic reaction centers. Clear imaging of the environment surrounding the dopant site could yield new insights into proposed reaction mechanisms and pathways. However, direct observation of single-atom reaction centers for photocatalytic hydrogen production has not yet been reported.

In this work, we report the direct observation of isolated Rh atoms in Rh-doped titania single-crystal nanosheets with uniform thickness of 0.7 nm and show that, for appropriate

Received: October 1, 2014
Published: December 5, 2014

   dx.doi.org/10.1021/ja509970z | J. Am. Chem. Soc. 2015, 137, 239−244

dopant concentrations, the photocatalytic activity can be significantly increased. Additionally, we present density functional theory simulations to understand the mechanism for the increased photocatalytic activity when isolated Rh atoms are present as dopants at the surface.

EXPERIMENTAL SECTION

Materials. $CsCO_3$ (95.0%, Wako Pure Chemical Industries Ltd.), TiO_2 (99.0%, Wako Pure Chemical Industries Ltd.), and $RhCl_3 \cdot 3H_2O$ (99.5%, Wako Pure Chemical Industries Ltd.) were used for preparation of samples.

Nanosheet Preparation. The parent layered oxides, $Cs_{0.7}Ti_{1.82-x}Rh_xO_4$ (x = 0–0.09), were prepared from $CsCO_3$, TiO_2, and $RhCl_3 \cdot 3H_2O$. A mixture of these reagents was added to 50 mL of water, after which the water was evaporated by heat treatment. The mixture was calcined in air at 673 K for 1 h, and then ground and calcinated at 1073 K for 20 h. This process was repeated two times. $Cs_{0.7}Ti_{1.82-x}Rh_xO_4$ (0.5 g) was converted into the protonated form by acid-exchange processing in a 0.1 M HCl solution (50 mL) for 3 days. After protonation, the powder was washed during several centrifugation steps. The sediment (powder paste) obtained after centrifugation (0.0236 g) was stirred in a 0.025 M tetrabutylammonium hydroxide aqueous solution (50 mL) for 1 week to form a colloidal nanosheet suspension. The doping amount in the nanosheet was determined by ICP measurement.

Photocatalytic Reactions. Photocatalysis experiments were performed using a conventional closed circulation system. A quartz reaction cell was irradiated by light from an external light source (500 W Xe lamp). The production of H_2 was quantified by gas chromatography with a thermal conductivity detector, which was connected to a conventional volumetric circulating line. Methanol aqueous solution (20 vol%) was used as the reaction solution. The amount of catalyst was 20 mg.

Characterization and Equipment. The crystal structure of the nanosheets was analyzed by X-ray powder diffraction (Cu Kα radiation; Rigaku, RINT-2500). High-angle annular dark-field scanning transmission electron microscopy (HAADF-STEM) images were obtained using JEOL JEM-ARM200F microscopes. The HAADF images were simulated using the software Mac TempsX. X-ray absorption near-edge structure (XANES) and extended X-ray absorption fine structure (EXAFS) of the Rh-based samples were measured at the Photon Factory light source, a part of the High Energy Accelerator Research Organization (Proposal No. 2012G593). Rh K-edge XANES/EXAFS spectra for the samples were obtained using a Si(311) two-crystal monochromator with beamline NW10A. These spectra were measured in transmission mode at room temperature. Analysis of the EXAFS data was performed using the EXAFS analysis program, REX (Rigaku Co.). A Fourier transform of the k^3-weighted Rh K-edge EXAFS oscillation was performed over the k range from 4 to 15 $Å^{-1}$. Inverse Fourier-transformed data for the Fourier peaks were analyzed using a curve-fitting method including phase shift and amplitude functions using the spectroscopy software FEFF 8.0.

Density Functional Theory Simulations. The DFT results presented here were obtained using the VASP code,[19,20] projector-augmented wave pseudopotentials,[21,22] and the PBE approximation[23] to the exchange correlation functional. The Kohn–Sham orbitals are expanded in plane waves using an energy cutoff of 400 eV, and 48-atom supercells of pristine (undoped) and doped lepidocrocite nanosheets are simulated using a slab model. A 15 Å vacuum region is included to prevent spurious interactions between neighboring nanosheets.

RESULTS AND DISCUSSION

The parent layered oxide $Cs_{0.7}Ti_{1.82-x}Rh_xO_4$ has a layered structure with a titanium oxide host layer and guest Cs ions (see Supporting Information, Figure S1). Undoped $Cs_{0.6}Ti_{1.84}O_4$ has a body-centered orthorhombic crystal structure (*Immm*).[24] All XRD patterns for the doped $Cs_{0.7}Ti_{1.82-x}Rh_xO_4$ were consistent with those of undoped $Cs_{0.7}Ti_{1.82}O_4$, with some modifications induced by the dopants. The diffraction angles assigned to the (200) face increased, while the angle for the (020) face decreased (see Supporting Information, Figure S2). The angle for the (002) faces did not change. These results indicate that doping of Rh results in shrinkage of the a axis and expansion of the b axis.

Exfoliation of the layered titanium oxide to single nanosheets was confirmed by atomic force microscopy (AFM; see Supporting Information, Figure S3). In theory, the nanosheet has a lepidocrocite-like structure with a thickness of 0.7 nm, and some quantity of defects may exist at the Ti sites, a structural model for which is shown in Figure 1. According to

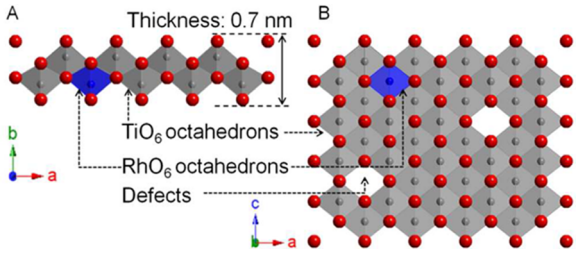

Figure 1. Structural models of Rh-doped titania nanosheet: (A) sectional view and (A) plan view.

the AFM image, the nanosheet was approximately 1.0 nm thick, which corresponds well to the theoretical value. This indicates that the Rh-doped layered titanium oxide was completely exfoliated into a monolayer nanosheet. Due to its ionic radius and valence, Rh atoms are expected to occupy Ti sites in the nanosheet lattice in the Rh^{3+} state, but this was difficult to confirm from the XRD pattern. Other possibilities that require consideration include the formation of Rh clusters within the crystal, the occupation of crystal sites other than Ti^{4+} sites, or the incorporation of Rh atoms as interstitials or at defect sites. Therefore, HAADF-STEM was used for direct observation of the Rh atoms in the nanosheet.

Figure 2a shows a HAADF-STEM image of a Rh (x = 0.026)-doped $Ti_{1.82-x}Rh_xO_4$ nanosheet. The HAADF detector collects electrons that undergo high-angle scattering, and the signal intensity is approximately proportional to Z^2, where Z is the atomic number.[25] Therefore, the contrast in the HAADF-STEM image enables the identification of Rh (Z = 45) and Ti (Z = 22) ions in the nanosheet. Furthermore, in the case of a single layer nanosheet where the electron beam interacts with only one species throughout the thickness of the sample, it is easy to determine if and where Rh dopant atoms are present. Therefore, it is reasonable to conclude that the brightest spots in the image represent Rh atoms, and the spots with intermediate brightness represent Ti atoms. (Due to their low atomic number (Z = 8), O atoms are not visible in the image.) Yellow arrows in Figure 2a indicate that isolated Rh atoms distributed within the Ti host sites. Figure 2b shows a magnified image for Rh-doped nanosheet, also showing a Rh atom at the brightest spot. Figure 2c shows a color-coded intensity map derived from Figure 2b, where the contrast is adjusted to highlight the dopant atom. The atomic structural model corresponding to Figure 2b is shown in Figure 2d, which consists of 1 Rh atom, 28 Ti atoms, and 3 vacancy-like defects. Figure 2e shows the HAADF-STEM image calculated from the structural model, which was simulated based on the frozen

dx.doi.org/10.1021/ja509970z | J. Am. Chem. Soc. 2015, 137, 239–244

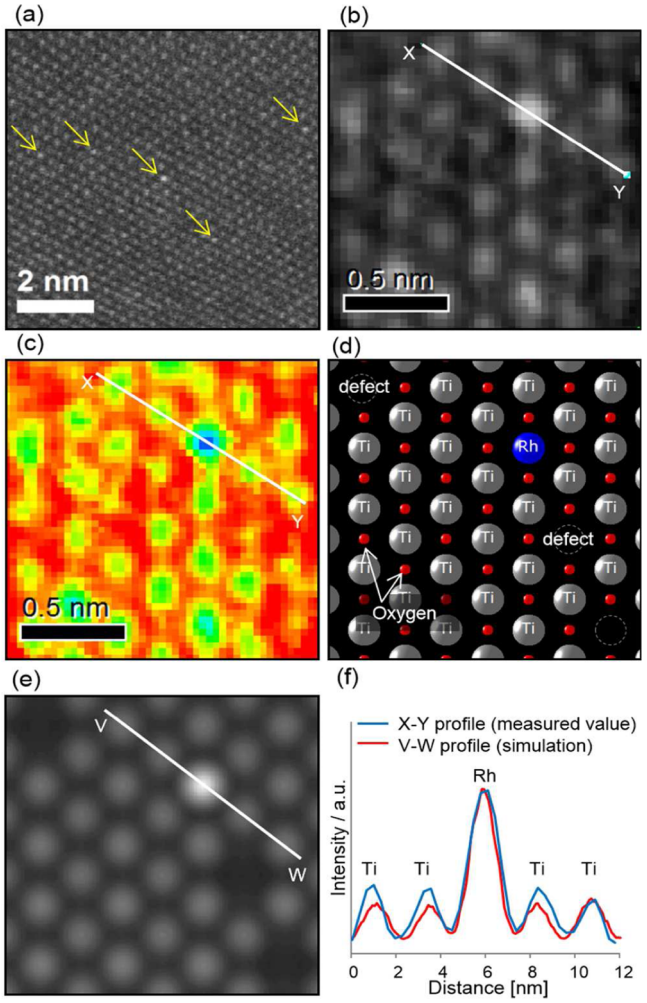

Figure 2. (a) HAADF-STEM (200 kV) image of Rh (x = 0.026)-doped $Ti_{1.82-x}Rh_xO_4$ nanosheet, (b) magnified HAADF-STEM image (80 kV) of Rh (x = 0.026)-doped nanosheet, (c) color-coded intensity map derived from panel b, (d) structural model expected from panel b, (e) HAADIF-STEM image simulated from the structural model described in panel d using frozen phonon model, and (f) intensity profiles along the line X−Y in the actually observed image (panel b) and the line V−W in the simulated image (panel e).

phonon model. Figure 2f shows the intensity profiles along the line X−Y in the observed image (Figure 2b) and the line V−W in the simulated image (Figure 2e). It should be noted that intensity map and profile in the simulated image are almost the same as those in the observed image. In the both images, the intensity for Rh atoms is approximately three times stronger than that for Ti atoms. These results indicate that Rh atoms are introduced as isolated dopants at the Ti^{4+} sites in the nanosheet lattice. We note also that, although the portions of the nanosheet upon which the electron beam was incident were easily destroyed during the image acquisition, other parts of the structure remained intact for further analysis.

XANES and EXAFS of the Rh-doped nanosheets were measured to determine the local structure of the doped Rh over a large area, since the TEM images provide only local information in a microscopic region. Figure 3 shows Rh K-edge XANES spectra for Rh-doped $Ti_{1.82-x}Rh_xO_4$ nanosheets with x = 0.026, RhO_x-loaded nanosheets, and reference samples (Rh foil and Rh_2O_3). In the RhO_x-loaded nanosheet, RhO_x nanoparticles were photo-deposited on the titania nanosheet.

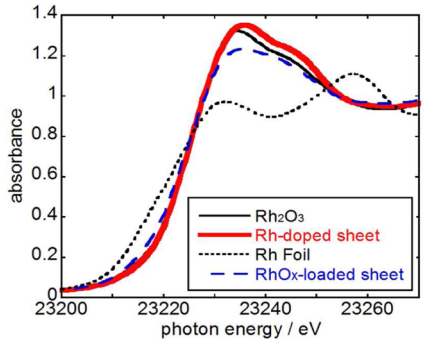

Figure 3. Rh K-edge XANES spectra for Rh (x = 0.026)-doped $Ti_{1.82-x}Rh_xO_4$ nanosheet (Rh-doped sheet), RhO_x-loaded $Ti_{1.82}O_4$ nanosheet (RhO_x-loaded sheet), and reference samples (Rh foil and Rh_2O_3).

The XANES absorption threshold for both the Rh-doped nanosheet and the Rh-loaded nanosheet is consistent with that of the XANES spectrum for Rh_2O_3, while by comparison the threshold of the Rh foil is located at lower energy. This confirms that Rh species in both samples exist in a similar chemical environment as in Rh_2O_3, and thus are oxidized. Furthermore, it should be noted that the white line for Rh-doped samples was more intense than that for RhO_x-loaded samples and Rh_2O_3. In addition, compared to the threshold for Rh_2O_3, the threshold for the Rh-doped samples was positioned at slightly higher energy, whereas the threshold for the RhO_x-supported samples was positioned at slightly lower energy. This suggests that the Rh species in the Rh-doped samples are more highly oxidized. This could occur, for instance, if some electrons in the Rh species are transferred to Ti cations via lattice oxygen in the Rh-doped samples (or alternatively if a small portion of the Rh species in RhO_x-supported samples exist in a reduced state).

Figure 4a shows Fourier transforms of Rh K-edge k^3-weighted EXAFS for Rh-doped and RhO_x-loaded titania nanosheet samples. For both the spectra, two peaks are observed at around 1.8 and 2.8 Å. Since Rh species in both samples are oxidized, the peak at 1.8 Å in both spectra arises from nearest neighbor interactions (the Rh−O bonds). In order to identify the surroundings in the second shell around the Rh atoms, the second peaks at around 2.8 Å were inverse Fourier-transformed, and the spectra thus obtained were fitted using phase shift and amplitude functions derived from the FEFF 8.0 software package.

Figure 4b shows inverse Fourier-transformed spectra for Rh-doped samples and RhO_x-supported samples for the peak at around 2.8 Å in Figure 4a. The envelope of the spectrum for Rh-doped samples is different from that of the RhO_x-loaded samples. The maximum in the envelope for the Rh-doped samples is located at around k = 7 $Å^{-1}$, while the maximum in the envelope for the spectra of RhO_x-loaded samples occurs at around 9 $Å^{-1}$. In general, the shape of the spectrum is influenced by the mass number of the neighboring atoms, with maxima in the envelope for light atoms appearing at smaller k, and that of heavy atoms appearing at larger k. Therefore, the transformed spectra are consistent with our expectations that the second shell comprises of Rh−Rh interactions in the RhO_x-loaded samples, while correspondingly in the doped Rh samples second-shell interactions feature lighter atoms, that is, Ti atoms. Table 1 shows the results on the curve-fitting analyses of the EXAFS. The peak for the Rh-doped samples is well fitted using

dx.doi.org/10.1021/ja509970z | J. Am. Chem. Soc. 2015, 137, 239−244

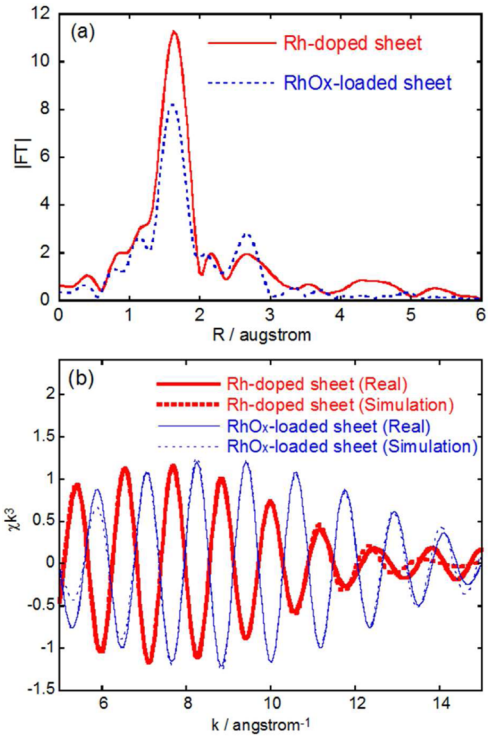

Figure 4. (a) Fourier transforms of Rh K-edge k^3-weighted EXAFS for Rh (x = 0.026)-doped and RhO_x-loaded titania nanosheet. (b) Inversely Fourier-transformed spectra for Rh-doped nanosheet and RhO_x-loaded nanosheet for the peak at around 2.8 Å in panel a.

Table 1. Curve-Fitting Analyses of the EXAFS

sample	shell	CN[a]	R^b/Å	σ^c/ Å
Rh-doped sheet	Rh−Ti	2.4 ± 0.3	3.11	0.094
Rh-loaded sheet	Rh−Ti	0.5 ± 0.2	2.93	0.063
	Rh−Rh	0.9 ± 0.2	3.04	0.071

[a]Coordination number. [b]Bond distance. [c]Debye−Waller.

a single shell of Rh−Ti, as shown in Figure 4b. In contrast, two shells of Rh−Rh and Rh−Ti were required to fit the EXAFS spectra for the Rh-loaded samples. Thus, it is likely that Rh atoms in the Rh-doped samples are located in the nanosheet lattice, while very small RhO_x particles are supported on the nanosheet surfaces in the loaded Rh samples. Overall, the EXAFS results strongly suggest that Rh is incorporated in the nanosheet not in the form of clusters but as individual, isolated atoms.

Having established the atomic-scale structure of the Rh-doped nanosheets, we measured the photocatalytic activity of sheets doped to different degrees. Figure 5 shows the photocatalytic activity of for H_2 production as a function of the amount of Rh doping (Rh/(Ti+Rh) = 0−4%). The H_2 production rate for the undoped nanosheet was very low, whereas the Rh-doped nanosheets exhibited a high hydrogen production rate. Interestingly, the activity exhibits a maximum around 1.4% doping, with the H_2 production rate (51 μmol/h) about 10 times that of the undoped nanosheet (5 μmol/h). We speculate that one reason for the maximum in the activity at this concentration could be that the Rh dopants serve a dual function, both as reaction centers and recombination centers. For low doping, the function as a reaction center is dominant, but for high doping the contribution of the recombination

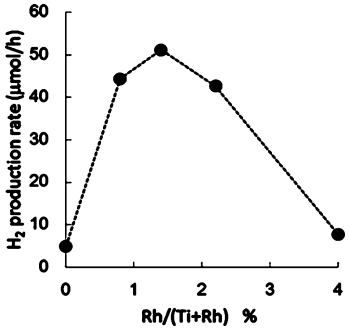

Figure 5. Photocatalytic activity of $Ti_{1.82-x}Rh_xO_4$ nanosheet for H_2 production as a function of the amount of Rh doping. The photocatalytic hydrogen production was performed from 20 vol% methanol aqueous solutions.

center function becomes dominant and limits overall H_2 production. Overall, these results support the idea that single Rh atoms in the two-dimensional titanium oxide crystal can function as co-catalysts for the reduction of water into hydrogen. Therefore, the smallest RhO_x co-catalyst that can function as a reduction site for water is a single atom. We also note that the Rh-doped nanosheet showed high catalytic activity compared with the RhO_x-loaded nanosheet (see Supporting Information, Figure S5). The maximum H_2 production rate of the RhO_x-loaded TiO_2 nanosheet (33 μmol/h, (Rh/(Ti+Rh) = 4.6%)) was lower than that of Rh-doped TiO_2 nanosheet.

To understand the mechanism for the photocatalytic activity of the doped nanosheets, we carried out density functional theory[26,27] simulations. For lepidocrocite TiO_2, the initial adsorption of water molecules atop the surface is believed to be a rate limiting step since water molecules are not believed to bind favorably to the undoped lepidocrocite surface.[28] Therefore, we explore this initial adsorption step in detail. In agreement with previously reported results,[28] we also find that water molecules do not interact with the undoped lepidocrocite surface (regardless of initial configuration, they are always pushed away from the surface during the relaxation; see Figures 6 and 7, initial state). This is not surprising since the surface Ti atoms are fully six-fold coordinated, and is also the case even when Rh dopant atoms are present.

On the other hand, our simulations reveal a metastable dissociatively adsorbed state for both the doped and the undoped system. The atomic configuration of the dissociated states is similar for both cases (Figures 6 and 7, final configuration), with an OH fragment adsorbed atop a (now seven-fold coordinated) Ti atom and the H atom adsorbed atop a surface bridging oxygen. Despite the similar geometries, the total energy cost for dissociation is 0.85 eV in the undoped system, but only 0.48 eV when dissociated near the Rh atom. The different energy cost of dissociation, 0.85 eV vs 0.48 eV, suggests that more dissociated water molecules can be found when the nanosheets are doped. From the Boltzmann factor based on this difference, we can expect ∼6 times more dissociated water molecules on the Rh-doped systems than the undoped systems.

In addition to the total energy change, we also estimated the reaction pathway and barrier using the nudged elastic band method. Quite surprisingly, the simulations reveal that the transition barrier itself is actually larger (1.40 eV vs 0.98 eV) in the presence of Rh dopants. The geometry of the transition

dx.doi.org/10.1021/ja509970z | J. Am. Chem. Soc. 2015, 137, 239−244

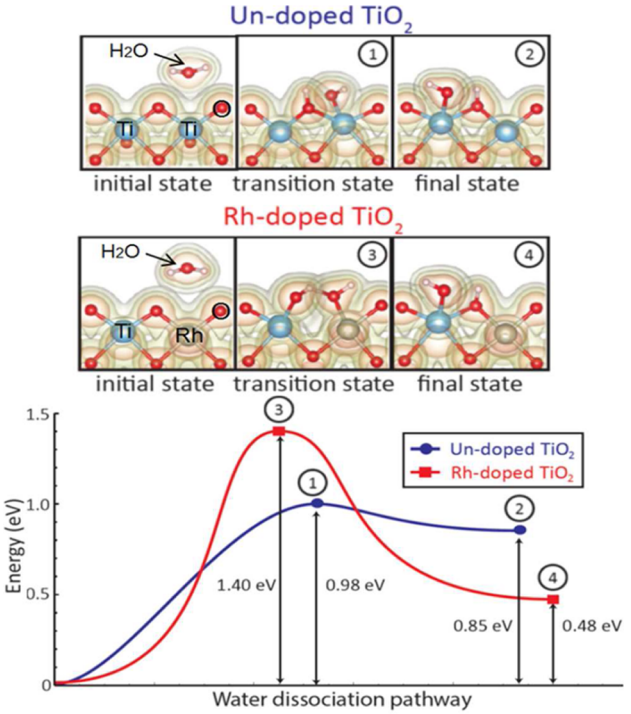

Figure 6. Charge density and dissociation energetics for undoped and Rh-doped titania nanosheet.

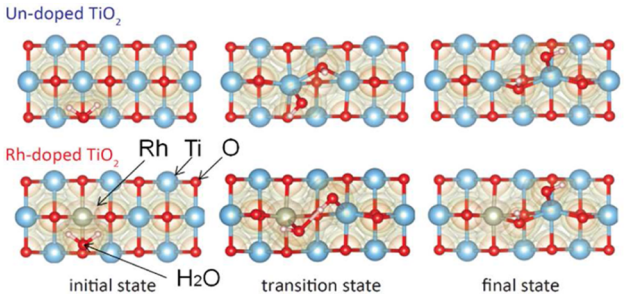

Figure 7. Top view images for charge density of nanosheet during water dissociation process for undoped and Rh-doped nanosheets.

state, and the energy barrier are indicated in Figures 6 and 7. The transition-state geometry is quite different for the two systems. For the undoped systems, as the H_2O approaches the surface the O atom binds with a surface six-fold-coordinated Ti atom and one H atom binds to a surface bridging oxygen atom. As this takes place, the OH bond elongates and ultimately breaks, and the associated energy barrier is 0.98 eV. Small relaxations to the dissociated geometry recover a small energy giving a total dissociation energy of 0.85 eV. By contrast, for the doped system, at the transition state the bond between the surface bridging oxygen atom and the rhodium atom is already broken and the bridging oxygen atom has lifted away from the surface. Despite the higher barrier, the relaxations that take place beyond the transition state are more substantial (and re-form the broken surface bond) and result in a dissociated energy of only 0.48 eV.

The larger reaction barrier for the doped system is initially surprising, and we consider three possibilities here. Admittedly, one possibility is that there is a lower energy pathway for the doped system that our simulations did not find. We did, however, trace the energy landscape for the doped system using the reaction coordinates of the undoped system, and we found the barrier to be much higher (~3 eV). This suggests that the dissociation mechanism on the doped sheet should be different from that on the undoped sheet.

Second, in any case the relative portion of adsorbed molecules present on the surface depends on the total energy change itself rather than the barriers. Although the rate of the forward reaction (dissociative adsorption) is slower for the doped system, the rate of the backward reaction (desorption) is much faster (compare the barrier of 0.13 eV to 0.92 eV). Considering both the rate of the forward and backward reaction together, the total rate depends only on the total reaction energy and thus favors the doped system. We note that in the present photocatalytic reaction, TiO_2 is excited by light irradiation with energy >3.5 eV. This energy is much larger than the reaction barriers for both the undoped (0.98 eV) and the Rh-doped (1.4 eV) systems so both systems have sufficient energy to climb the barrier.

Finally, we note that water dissociation at the surface as in state 2 or 4 (Figure 6) is not the final state (generation of H_2), but only a reaction intermediate state. In the full reaction pathway to the final state, at least one or more transition sates exist that may influence the overall rate. The study on the full reaction pathway for hydrogen production is currently in progress.

In conclusion, a Rh-doped titania nanosheet was prepared. The photocatalytic activity for hydrogen production from this nanosheet was 10 times that for an undoped nanosheet. The presence of single Rh atoms substituting for Ti^{4+} in the nanosheet lattice was confirmed by TEM observation. This indicates that single Rh atoms can act as reaction centers for the photocatalytic reaction. Thus, crystal sites containing a single transition metal atom in the photocatalyst can act as a co-catalyst. The experimental observations are supported by first-principles modeling methods. These results will be useful in better understanding the role of the co-catalyst and the mechanism, and will provide new insight for the design of advanced photocatalysts for water splitting.

■ ASSOCIATED CONTENT

Supporting Information

Structural model for preparation process of Rh-doped titania nanosheets (Figure S1), XRD patterns of Rh-doped $Cs_{0.7}Ti_{1.82}O_4$ (Figure S2), AFM image of Rh-doped nanosheet (Figure S3), XPS spectra of Rh-doped titania nanosheet (Figure S4), and photocatalytic activity of RhO_x-loaded titania nanosheet (Figure S5). This material is available free of charge via the Internet at http://pubs.acs.org.

■ AUTHOR INFORMATION

Corresponding Authors

s-ida@cstf.kyushu-u.ac.jp
ertekin@illinois.edu

Notes

The authors declare no competing financial interest.

■ ACKNOWLEDGMENTS

This work was supported by JST PRESTO program and JSPS KAKENHI 24685031. The authors gratefully acknowledge the support of the International Institute for Carbon Neutral Energy Research (WPI-I2CNER), sponsored by the World Premier International Research Center Initiative (WPI),

MEXT, Japan. Computational resources were provided by (i) the Extreme Science and Engineering Discovery Environment (XSEDE) allocation DMR-140007, which is supported by National Science Foundation grant number ACI-1053575, and (ii) the Illinois Campus Computing Cluster. We thank T. Daio for discussion about STEM data.

REFERENCES

(1) Bard, A. J.; Fox, M. A. *Acc. Chem. Res.* **1995**, *28*, 141.
(2) Zou, Z.; Ye, J.; Sayama, K.; Arakawa, H. *Nature* **2001**, *414*, 625.
(3) Khan, S. U. M.; Al-Shahry, M.; Ingler, W. B., Jr. *Science* **2002**, *297*, 2243.
(4) Kanan, M. W.; Nocera, D. G. *Science* **2008**, *321*, 1072.
(5) Kudo, A.; Miseki, Y. *Chem. Soc. Rev.* **2009**, *38*, 253.
(6) Kato, H.; Asakura, K.; Kudo, A. *J. Am. Chem. Soc.* **2003**, *125*, 3082.
(7) Maeda, K.; Takata, T.; Hara, M.; Saito, N.; Inoue, Y.; Kobayashi, H.; Domen, K. *J. Am. Chem. Soc.* **2005**, *127*, 8286.
(8) Maeda, K.; Domen, K. *J. Phys. Chem. Lett.* **2010**, *1*, 2655.
(9) Higashi, M.; Abe, R.; Teramura, K.; Takata, T.; Ohtani, B.; Domen, K. *Chem. Phys. Lett.* **2008**, *452*, 120.
(10) Ye, J.; Zou, Z.; Oshikiri, M.; Matsushita, A.; Shimoda, M.; Imai, M.; Shishido, T. *Chem. Phys. Lett.* **2002**, *356*, 221.
(11) Sasaki, T.; Watanabe, M. *J. Am. Chem. Soc.* **1998**, *120*, 4682.
(12) Schaak, R. E.; Mallouk, T. E. *Chem. Mater.* **2000**, *12*, 3427.
(13) Ebina, Y.; Sakai, N.; Sasaki, T. *J. Phys. Chem. B* **2005**, *109*, 17212.
(14) Hata, H.; Kobayashi, Y.; Bojan, V.; Justin Youngblood, W.; Mallouk, T. E. *Nano Lett.* **2008**, *8*, 794.
(15) Comptons, O. C.; Mullet, C. H.; Chiang, S.; Osterloh, F. E. *J. Phys. Chem. C* **2008**, *112*, 6202.
(16) Ida, S.; Okamoto, Y.; Matsuka, M.; Hagiwara, H.; Ishihara, T. *J. Am. Chem. Soc.* **2012**, *134*, 15773.
(17) Ida, S.; Takashiba, A.; Koga, S.; Hagiwara, H.; Ishihara, T. *J. Am. Chem. Soc.* **2014**, *136*, 1872.
(18) Ebina, Y.; Sasaki, T.; Harada, M.; Watanabe, M. *Chem. Mater.* **2002**, *14*, 4390.
(19) Kresse, G.; Hafner, J. *Phys. Rev. B* **1993**, *47*, 558.
(20) Kresse, G.; Hafner, J. *Phys. Rev. B* **1994**, *49*, 14251.
(21) Kresse, G.; Joubert, D. *Phys. Rev. B* **1999**, *59*, 1758.
(22) Blöchl, P. E. *Phys. Rev. B* **1994**, *50*, 17953.
(23) Perdew, J. P.; Burke, K.; Ernzerhof, M. *Phys. Rev. Lett.* **1996**, *77*, 3865.
(24) Grey, I. E.; Li, C.; Madsen, I. C.; Watts, J. A. *J. Solid State Chem.* **1987**, *66*, 7.
(25) Pennycook, S. J.; Boatner, L. A. *Nature* **1988**, *336*, 565.
(26) Hohenberg, P.; Kohn, W. *Phys. Rev.* **1964**, *136*, B864.
(27) Kohn, W.; Sham, L. J. *Phys. Rev.* **1965**, *140*, A1133.
(28) Casarin, M.; Vittadini, A.; Selloni, A. *ACS Nano* **2009**, *3*, 317.